Acta Neuropathol (2009) 118:763–776
DOI 10.1007/s00401-009-0589-x

ORIGINAL PAPER

The dorsal root ganglion in Friedreich's ataxia

Arnulf H. Koeppen · Jennifer A. Morral · Ashley N. Davis · Jiang Qian · Simone V. Petrocine · Mitchell D. Knutson · Walter M. Gibson · Matthew J. Cusack · Danhong Li

Received: 14 July 2009 / Revised: 22 August 2009 / Accepted: 23 August 2009 / Published online: 30 August 2009

Abstract Atrophy of dorsal root ganglia (DRG) and thinning of dorsal roots (DR) are hallmarks of Friedreich's ataxia (FRDA). Many previous authors also emphasized the selective vulnerability of larger neurons in DRG and thicker myelinated DR axons. This report is based on a systematic reexamination of DRG, DR and ventral roots (VR) in 19 genetically confirmed cases of FRDA by immunocytochemistry and single- and double-label immunofluorescence with antibodies to specific proteins of myelin, neurons and axons; S-100α as a marker of satellite and Schwann cells; laminin; and the iron-responsive proteins ferritin, mitochondrial ferritin, and ferroportin. Confocal images of axons and myelin allowed the quantitative analysis of fiber density and size, and the extent of DR and VR myelination. A novel technology, high-definition X-ray fluorescence (HDXRF) of polyethylene glycol-embedded fixed tissue, was used to "map" iron in DRG. Unfixed frozen tissue of DRG in three cases was available for the chemical assay of total iron. Proliferation of S-100α-positive satellite cells accompanied neuronal destruction in DRG of all FRDA cases. Double-label visualization of peripheral nerve myelin protein 22 and phosphorylated neurofilament protein confirmed the known loss of large myelinated DR fibers, but quantitative fiber counts per unit area did not change. The ratio of myelinated to neurofilament-positive fibers in DR rose significantly from 0.55 to 0.66. In VR of FRDA patients, fiber counts and degree of myelination did not differ from normal. Pooled histograms of axonal perimeters disclosed a shift to thinner fibers in DR, but also a modest excess of smaller axons in VR. Schwann cell cytoplasm in DR of FRDA was depleted while laminin reaction product remained prominent. Numerous small axons clustered around fewer Schwann cells. Ferritin in normal DRG localized to satellite cells, and proliferation of these cells in FRDA caused wide rims of reaction product about degenerating nerve cells. Mitochondrial ferritin was not detectable. Ferroportin was present in the cytoplasm of normal satellite cells and neurons, and in large axons of DR and VR. In FRDA, some DRG neurons lost their cytoplasmic ferroportin immunoreactivity, whereas the cytoplasm of satellite cells remained ferroportin positive. Ferroportin in DR axons disappeared in parallel with atrophy of large fibers. HDXRF of DRG detected regional and diffuse increases in iron fluorescence that matched ferritin expression in satellite cells. The observations support the conclusions that satellite cells and DRG neurons are affected by iron dysmetabolism; and that regeneration and inappropriate myelination of small axons in DR are characteristic of the disease.

Keywords Dorsal root ganglia · Ferritin · Ferroportin · Friedreich's ataxia · Iron · Spinal nerve roots

Walter M. Gibson: Deceased.

A. H. Koeppen (✉) · J. A. Morral · A. N. Davis
Research Service (151), Veterans Affairs Medical Center,
113 Holland Ave, Albany, NY 12208, USA
e-mail: arnulf.koeppen@med.va.gov

A. H. Koeppen
Department of Neurology,
Albany Medical College, Albany, NY, USA

A. H. Koeppen · J. Qian · S. V. Petrocine
Department of Pathology and Laboratory Medicine,
Albany Medical College, Albany, NY, USA

M. D. Knutson
Food Science and Human Nutrition Department,
University of Florida, Gainesville, FL, USA

M. J. Cusack · D. Li
X-ray Optical Systems, East Greenbush, NY, USA

Introduction

Friedreich's ataxia (FRDA) represents a complex pathological phenotype involving heart, pancreas, skeleton, and the central and peripheral nervous systems (reviewed in ref. [16]). Friedreich completed autopsies in four of his patients and in 1877 summarized his findings in a post scriptum to his four prior articles [9]. He emphasized atrophy of the spinal cord and offered the first illustrations of the lesions in dorsal and lateral columns. He also recognized neuronal loss in the dorsal nuclei of Clarke and thinning of dorsal roots (DR). He thought that dorsal root ganglia (DRG) were normal. The critical role of DRG in the pathology of FRDA did not become apparent until the meticulous study of a single case by Mott [26]. Most subsequent neuropathological examinations confirmed overall reduction in the size of DRG, atrophy or active destruction of nerve cells, "residual nodules" [2] (also known as nodules of Nageotte [27]), and gray discoloration of the thinned DR. Myelin stains confirmed the loss of larger myelinated fibers in DR, but early authors could not properly conclude that the remaining thinner fibers were devoid of myelin or only thinly myelinated. Lambrior [20] used a precursor method to more recent teased-fiber technology and observed loss of large myelinated fibers in DR. Most students of FRDA thought that the density of axons in DR remained normal, and Jitpimolmard et al. [14] also made the observation that DR of FRDA patients contained regenerative clusters. Ventral roots (VR) were generally preserved, although Lambrior [20] commented on interspersed thin fibers among the larger axons.

Friedreich's ataxia (FRDA) is now defined by its genetics rather than its clinical or neuropathological phenotypes [4], and the identity of the disease in several early neuropathological descriptions has become somewhat uncertain. This report is based on a systematic analysis of 19 genetically confirmed autopsy cases of FRDA in which DRG were available for study. The study included the determination of axonal density and degree of myelination in DR and VR; visualization of S-100α as a marker of satellite cells in DRG and Schwann cell cytoplasm of DR and VR; and immunocytochemistry of laminin in DR and VR.

Friedreich's ataxia causes deficiency of frataxin, a small mitochondrial protein that participates in the biogenesis of iron–sulfur clusters. Iron–sulfur clusters are needed for the proper function of complexes I, II, and III of the electron transport chain, and the citric acid cycle enzyme, aconitase (reviewed in refs. [28, 30]). The result of insufficient frataxin is impaired oxidative phosphorylation, but an additional factor in the pathogenesis of FRDA is iron-mediated oxidative damage. Routine iron stains of the heart in FRDA show the accumulation of blue granular reaction product in a small percentage of cardiomyocytes [19, 23], but proof of similar local iron excess in neural tissues is still outstanding. Therefore, this investigation also included a search for changes in the expression of three iron-responsive proteins, cytosolic ferritin, mitochondrial ferritin, and ferroportin. A novel technique was high-definition X-ray fluorescence (HDXRF) [6, 10], which allowed the detection and mapping of iron in tissue blocks, and subsequent matching with sections stained for ferritin.

Patients and methods

Basic clinical and genetic information

Table 1 lists basic information on 19 patients with FRDA. The ages of onset and death in years (mean ± standard deviation) were 10 ± 6 and 36 ± 18, respectively. The mean disease duration was 26 ± 14 years. The long survivors, FRDA 3 and FRDA 4, were sisters, and both had relatively short expansions in one allele. Cardiomyopathy was the main cause of death in 11 of 19 FRDA patients (57.9%) and contributed to death in five cases (26.3%). Only three FRDA patients, among them the two sisters with long survival (FRDA 3 and 4), had no clinical evidence of heart disease. Delay between death and tissue fixation ranged from 3 h to 3 days.

Slide techniques

Spinal cord and DRG were fixed in commercial buffered formaldehyde solution (4% w/v). Whenever possible, fixation over 2–4 weeks occurred at 4°C. The unfixed DRG of three FRDA patients were frozen at −75°C for iron assay.

Routine stains, immunocytochemistry, and immunofluorescence were made on 6-μm-thick paraffin sections. Transverse slices of the mid-lumbar spinal cord were embedded to represent as many cross-sections of DR and VR as possible. All DRG were harvested from lumbar and sacral spinal roots.

The following antisera (antibodies) for positive-contrast immunocytochemistry and single- and double-label laser confocal immunofluorescence were available from commercial sources: Monoclonal anti-class-III-β-tubulin (TUJ-1; R&D Systems, Minneapolis, MN, USA); monoclonal anti-S100α (Santa Cruz Biotechnology, Santa Cruz, CA, USA); polyclonal anti-peripheral nerve myelin protein 22 (PMP-22) (Abcam, Cambridge, MA, USA); monoclonal anti-phosphorylated neurofilament protein (SMI-31; Covance, Emeryville, CA, USA); monoclonal anti-myelin basic protein (MBP) (Covance); monoclonal anti-laminin (Sigma, St. Louis, MO, USA); polyclonal anti-human liver ferritin (DAKO, Carpinteria, CA, USA); and polyclonal

Table 1 Sex, ages of onset and death, cause of death, and guanine–adenine–adenine trinucleotide repeats in patients with Friedreich's ataxia (FRDA); age of death and cause of death in normal controls (*N*)

No.	Sex	Age of onset	Age of death	GAA repeats	Cause of death
FRDA 1	F	7	38	750/594	Cardiomyopathy, embolic stroke
FRDA 2	F	10	25	850/750	Cardiomyopathy
FRDA 3	F	22	65	631/242	Cachexia
FRDA 4	F	21	79	549/356	Cachexia, stroke
FRDA 5	F	10	24	950/700	Cardiomyopathy
FRDA 6	F	9	26	850/690	Cardiomyopathy
FRDA 7	M	16	39	491/370	Cardiomyopathy
FRDA 8	F	8	28	709/559	Cardiomyopathy, embolic stroke
FRDA 9	F	8	23	777/528	Cardiomyopathy, bronchopneumonia
FRDA 10	F	8	15	840/840	Cardiomyopathy
FRDA 11	F	17	58	566/566	Cardiomyopathy; brain hemorrhage
FRDA 12	M	10	38	934/249	Cardiomyopathy
FRDA 13	F	11	42	990/761	Cardiomyopathy
FRDA 14	F	7	55	793/644	Cachexia
FRDA 15	F	6	36	840/715	Cardiomyopathy
FRDA 16	F	2	33	604/455	Cardiomyopathy, renal failure
FRDA 17	M	2	10	1,016/1,016	Cardiomyopathy
FRDA 18	F	12	24	910/740	Myoglobinuria
FRDA 19	M	3	23	1,200/1,200	Cardiomyopathy
N 1	M		58		Carcinoma of the colon
N 2	M		77		Carcinoma of the lung
N 3	M		59		Multiple myeloma
N 4	M		61		Bacteremia
N 5	F		25		Carcinoma of the lung
N6	F		17		Congenital heart disease (ventricular septal defect)
N7	M		26		Fungal encephalitis
N8	F		38		Thrombotic thrombocytopenic purpura; cardiac arrest
N9	F		44		Carcinoma of the liver
N10	M		12		Pneumonia
N11	M		30		Rejection of heart transplant

anti-neurofilament H-chain protein (Sigma). A polyclonal anti-mouse ferroportin peptide antibody was available from Knutson et al. [15], and a rabbit polyclonal anti-human ferroportin peptide antibody was raised in a commercial laboratory to the first author's specifications. The amino acid sequence was NLHKDTEPKPLEGT. A C-terminal cysteine was added to permit linkage to keyhole limpet hemocyanin. The antibody was purified by affinity chromatography against the immobilized peptide. Dr. Sonia Levi, Milan, Italy, donated mouse polyclonal anti-mitochondrial ferritin. Optimal dilutions of antibodies were determined by trial and error (0.1–1 μg protein/ml). Secondary biotinylated antibodies to mouse or rabbit IgG (Vector Labs, Burlingame, CA, USA) were diluted to 0.6 μg protein/ml. Fluorescein isothiocyanate (FITC)-labeled secondary antibodies (Vector Labs) were used at 15 μg protein/ml. Horseradish peroxidase-labeled streptavidin (Sigma) was diluted to 0.4–2 μg protein/ml. Quantum dot 655 (Qdot655)-labeled streptavidin (Molecular Probes-Invitrogen, Carlsbad, CA, USA) was used at 3 μg protein/ml.

Tissue sections were deparaffinized and rehydrated by routine methods. Endogenous peroxidase was suppressed by exposure to 3% hydrogen peroxide in methanol when immunocytochemical detection included diaminobenzidine (DAB) and hydrogen peroxide as chromogens. Antigen retrieval varied with the tissue antigen of interest and subsequent processing of the sections for immunocytochemistry or immunofluorescence. Visualization of MBP and PMP-22 required an overnight incubation of the rehydrated slides in 80% ethanol at 4°C. Immunocytochemical and immunofluorescent reaction products of ferritin were improved by a 45-min-long chelation of sections in a solution of 2,2′-dipyridyl and sodium hydrosulfite (30 mM each) in 0.05 M acetate buffer (pH 4.8) prior to the application of the

antibody. For positive-contrast immunocytochemistry of class-III-β-tubulin, antigen retrieval consisted of heating the rehydrated sections in 0.01 M citrate buffer (pH 6) at 95°C for 3 min. Citrate buffer was also suitable for antigen retrieval of phosphorylated neurofilament protein. Laminin immunocytochemistry required digestion by trypsin (details in refs. [17, 23]) or proteinase K (Sigma). Proteinase K was applied at a concentration of 0.1 mg/ml in 0.02 M Tris buffer (pH 7.6) containing 100 mM NaCl (for 30 min at 37°C). A commercial antigen-retrieval preparation marketed under the trade name "DIVA" (Biocare Medical, Concord, CA, USA) was effective for the visualization of S-100α and ferroportin. It was also used for double-label immunofluorescence of the pairs: class-III-β-tubulin/ferritin and class-III-β-tubulin/ferroportin. Sections were heated at 95°C for 30 min in a diluted solution of DIVA (1:10 by vol).

The steps yielding immunocytochemical reaction product were described in detail before [17] and are summarized here as follows (washing steps omitted): Rehydration → background suppression with 10% normal horse serum in sodium phosphate buffered saline (pH 7.4) (PBS) containing 4% bovine serum albumin (BSA; w/v) → overnight incubation at 4°C in primary antibody (antiserum) in PBS containing 1% normal horse serum (by vol) and 4% BSA → biotinylated anti-rabbit (or mouse) IgG for 2 h at room temperature (RT) → incubation in HRP-streptavidin for 1 h at RT → incubation in DAB/hydrogen peroxide.

The protocol for single- and double-label immunofluorescence was similar to previously described procedures [17] although the "Quantum Red"-streptavidin of previous protocols [17, 23] was replaced by Qdot655-streptavidin. In the double-label protocol, incubation with monoclonal antibody was first (class-III-β-tubulin; phosphorylated neurofilament protein; S100α; MBP). The subsequent sequence was FITC-labeled anti-mouse IgG → a second suppression with normal horse serum → polyclonal antibody → biotinylated anti-rabbit IgG → Qdot655-labeled streptavidin. For confirmation of the result, the sequence was reversed for selected antigen combinations. The sections were viewed in a Meridian Insight confocal microscope (Okemos, MI, USA) under laser irradiation of 488 nm and filter settings of 530 ± 30 nm for FITC and 630 nm (long pass) for Qdot655. Single- and double-label digital images were recorded at magnifications of 40× and 100× for subsequent analysis.

Single-label fluorescence images of axons in DR and VR at 40× (phosphorylated neurofilament protein) were analyzed by a computer program to establish axonal counts/unit area and axonal perimeter, and to draw pooled histograms. The lower detection limit was set at a perimeter of 3.14 μm (1 μm diameter for perfectly round axonal profiles). Double-label images of nerve root myelin (PMP-22) and axons (phosphorylated neurofilament protein) were analyzed for the degree of myelination in DR and VR. The computer program was part of the confocal microscope and allowed separate displays of axons and myelin sheaths; exclusion of artifacts; placement of squares, circles, and triangles onto the images; and the separation of touching objects, such as tightly packed myelin sheaths. In 15 of the 19 patients with FRDA and in all 11 normal controls, sections of lumbar spinal cord were adequate to obtain digital images of five non-overlapping cross-sectional areas of DR and VR in each specimen. Data were analyzed by routine two sample t tests with a significance level of $\alpha = 0.05$.

HDXRF mapping of iron and spectroscopy

Gibson et al. [10] and Chen et al. [6] have previously described principles and applications of this new technology. Polyethylene glycol (PEG) infiltration of fixed DRG followed a standard protocol [18]. After full PEG infiltration, tissue blocks were "faced" in a microtome by cutting the blocks in steps of 25 μm with a Teflon-coated stainless steel blade until a smooth cut surface was achieved. Some of the sections were retained for routine iron histochemistry with Perls's reagents (1% potassium ferrocyanide in 1% hydrochloric acid). The available instrument for HDXRF consisted of an Oxford molybdenum (Mo) Apogee tube; a doubly curved crystal (DCC) monochromatic optic; a sample mount; translational stages; and a silicon drift detector. The X-ray source was operated at 50 W, and simple fan cooling was adequate for its efficient operation. The DCC allowed focusing of monochromatic Mo K_α X-rays to a slightly elliptical spot size of 85 × 90 μm. X-ray fluorescence was recorded at 60 μm steps while the sample was moved in raster-like manner until a complete iron "map" was generated. Copper and zinc fluorescence was recorded in the same session. Mapping was accomplished by exporting the data to a commercially available software package that ran in Microsoft Windows ("Origin", Origin Lab Corp., Northampton, MA, USA). After completion of HDXRF, the PEG-infiltrated tissue was recovered by washing out all PEG with PBS. The samples were then re-embedded in paraffin for the preparation of 6 μm-thick paraffin sections and ferritin immunocytochemistry. In DRG of four FRDA patients and two normal controls, iron maps and stained sections could be matched precisely to compare regions of iron fluorescence with ferritin reaction product.

Iron assay

Sufficient unfixed frozen DRG tissue of three patients with FRDA and eight normal controls was available for the assay of total iron. Correct sampling of DRG was assured

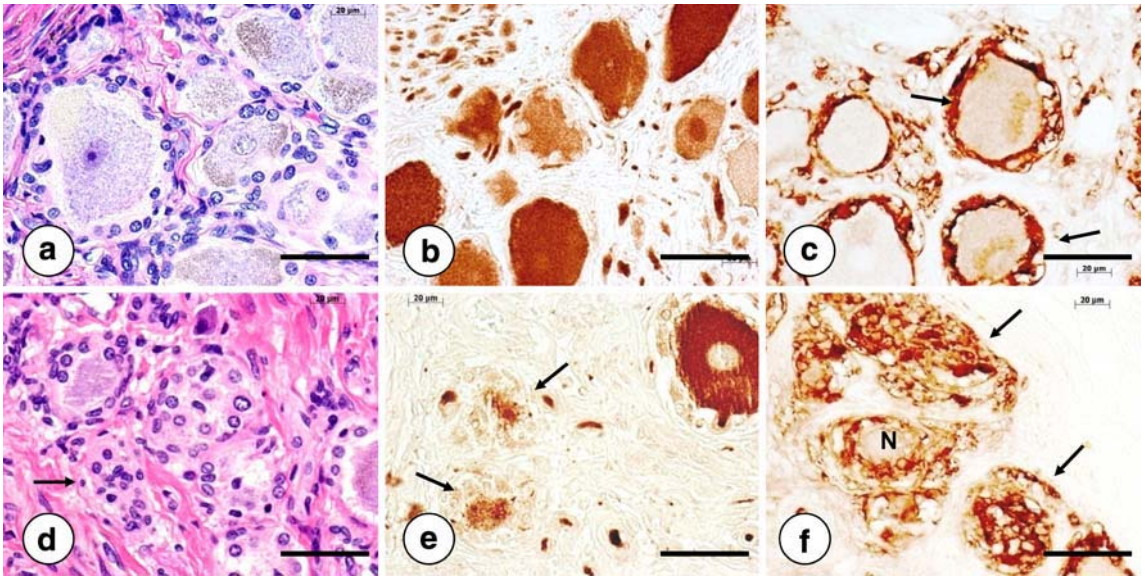

Fig. 1 The DRG in FRDA and a normal control: **a**–**c** normal DRG, **d**–**f** DRG in FRDA, **a**, **d** hematoxylin and eosin, **b**, **e** immunocytochemistry with monoclonal antibody TUJ-1 to class-III-β-tubulin, **c**, **f** immunocytochemical stain for S-100α. In the normal DRG (**a**–**c**), neurons are generally larger than in FRDA and display a single layer of satellite cells. In some neurons, satellite cells cause indentations of the neuronal cytoplasm (**b**). All ganglion cells exhibit reaction product with TUJ-1 although staining intensity varies. In FRDA (**d**), satellite cells seem to "invade" neurons, ultimately replacing them completely (*arrow* in **d**). TUJ-1 reaction product disappears in step with neuronal destruction (*arrows* in **e**). Satellite cells surrounding normal DRG neurons (**c**) show a relatively thin layer of perineuronal S-100α reaction product. In contrast, satellite cells of a DRG affected by FRDA are more numerous, and the boundary between these cells and neurons is indistinct ("*N*" in **f**). Nodules of Nageotte are strongly reactive with anti-S100α (*arrows* in **f**). *Magnification bars* 50 μm

by histological examination of immediately adjacent tissue. Digestion by sulfuric acid and ultrapure hydrogen peroxide, and colorimetric iron assay followed previously described protocols [17, 23]. The procedure was modified from Davis et al. [7] with ferrozine as the chromogenic substance.

Results

The first task in this work was an improved understanding of the pathological phenotype in DRG, DR, and VR. The second task was a search for evidence that the described abnormalities are due to iron dysmetabolism.

Morphological observations

DRG in FRDA

Figure 1 of DRG presents a comparison of FRDA and a normal control. The main process in FRDA is destruction of ganglion cells accompanied by a peculiar, invasion-like, replacement of neuronal cytoplasm by satellite cells (Fig. 1d, f). Nerve cell degeneration is especially apparent with an immunocytochemical stain for class-III-β-tubulin (Fig. 1e). Immunocytochemical staining of S-100α protein highlights the proliferation of satellite cells (Fig. 1f).

Dorsal and VR in FRDA

Figure 2 shows DR and VR in FRDA and a normal control after immunostaining with anti-PMP-22. The main abnormality in FRDA is a lack of larger myelinated fibers in DR (Fig. 2c, inset). Abundance and size of myelinated fibers in VR in FRDA appear unchanged (Fig. 2d) in comparison with the normal state (Fig. 2b).

Figure 3 is a composite of immunofluorescence of axons and a systematic histogram analysis of their perimeters. The digital images confirm the loss of large axons matching the disappearance of thicker myelin sheaths in DR (Fig. 2c). Large axons in VR of FRDA remain abundant, but small islands of very thin axons are also present (Fig. 3d). The pooled histograms in Fig. 3a′–d′ show the lack of larger axons in the DR of FRDA (Fig. 3c′), but also an excess of thinner axons in VR (Fig. 3d′).

Immunofluorescence of phosphorylated neurofilament protein (Fig. 3) also allowed precise determination of fiber density within the limitations of the technique. Axonal counts were, for DR, 8,966 ± 3,641 axons/mm^2 in 15 FRDA patients (mean ± standard deviation [SD]) and 9,040 ± 973 in 11 normal controls. For VR, fiber density was 5,565 ± 1,419 axons/mm^2 for the same FRDA patients and 4,849 ± 607 per mm^2 for the same normal controls. The differences are not statistically significant at $\alpha = 0.05$.

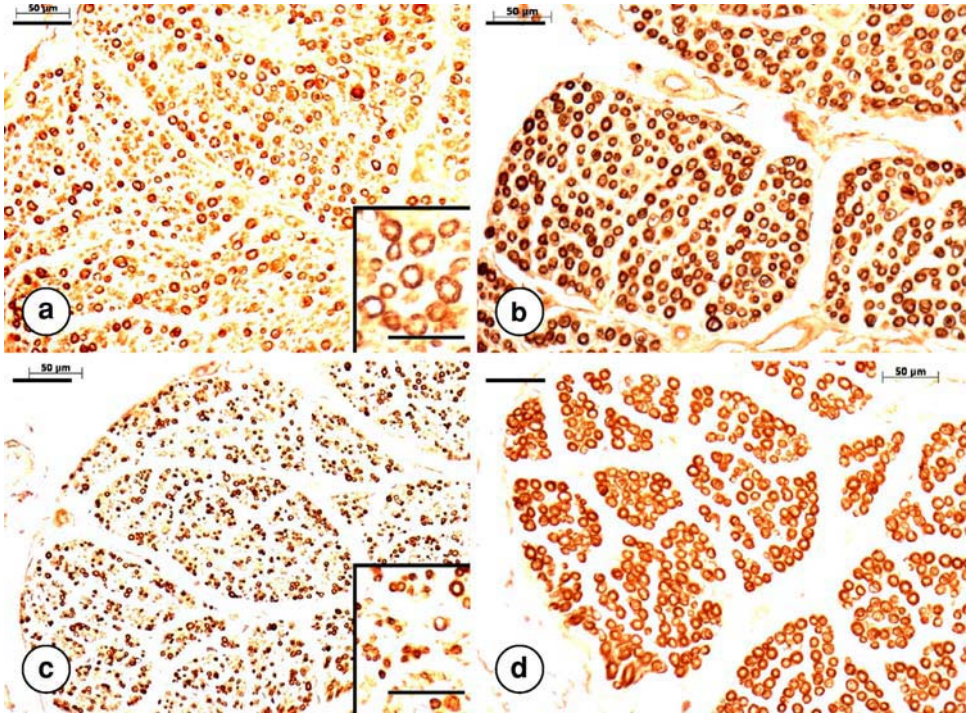

Fig. 2 Myelin in DR and VR of FRDA and a normal control. **a**, **b** Normal controls, **c**, **d** FRDA, **a**, **c** DR, **b**, **d** VR. The loss of large myelinated fibers in DR of FRDA is apparent (**c**, *inset*) when compared with the normal state (**a**, *inset*). Myelinated fibers in the DR of FRDA are very thin and very compact (**c**, *inset*). The VR in FRDA (**d**) does not visibly differ from the normal root (**b**). Immunocytochemistry with polyclonal anti-PMP22. *Magnification bars* 50 µm

Figure 4 illustrates double-label immunofluorescence of myelin with anti-PMP-22 and axons with an antibody to phosphorylated neurofilament protein. The lack of large myelinated fibers in DR of FRDA is apparent (Fig. 4c), but systematic computer-assisted analysis shows a significantly higher degree of myelination of DR in FRDA. The ratio of myelinated axons to all axons is 0.66 ± 0.16 (mean ± SD) in 15 FRDA patients; and 0.55 ± 0.16 in 11 normal controls ($p = 0.054$ at $\alpha = 0.05$). The ratios in VR on the same sections of spinal cord are not significantly different (FRDA, 0.76 ± 0.19; normal, 0.82 ± 0.15).

Figure 5 shows immunocytochemical staining of S-100α that was used to assess size and abundance of Schwann cells in DR and VR. Schwann cells are much smaller and less abundant in DR of FRDA, but the loss varies between patients (Fig. 5c, d). More severe depletion has occurred in a patient with a short guanine–adenine–adenine (GAA) trinucleotide repeat expansion on one allele and longer disease duration (Fig. 5d). The density of Schwann cells in VR of FRDA (Fig. 5e) does not appreciably differ from a normal control (Fig. 5b).

Figure 6 displays reaction product after staining with monoclonal anti-laminin. Although the epitope recognized by the antibody is not known, the reaction strongly stains Schwann cell basal laminas as evident in normal DR (Fig. 6a) and VR (Fig. 6b). The honeycomb-like appearance is due to negative images of large normal myelinated axons. In DR of FRDA (Fig. 6c), the distribution of laminin differs greatly from the normal state (Fig. 6a). Clusters of intense reaction product are widely separated from each other and surround thin nerve fibers shown as tiny circular voids in the reaction product (Fig. 6c). Laminin distribution in VR of a control (Fig. 6b) and FRDA (Fig. 6d) shows no differences.

Figure 7 extends the analysis of S-100α-reactive Schwann cells in DR and VR by inclusion of matching confocal images of axons. In VR of control and FRDA, each axon appears surrounded by Schwann cell cytoplasm, in an approximate 1:1 ratio. In normal DR, axonal profiles are much more numerous (Fig. 7b) than Schwann cell bodies (Fig. 7a). In Fig. 7e, representing DR of FRDA, S-100α reaction product is much less abundant than normal (Fig. 7a), presumably due to the loss of Schwann cell cytoplasm. The insets in Fig. 7e and f shows that axons cluster around the remaining larger Schwann cells. S-100α reaction product in Fig. 7a and e should also be compared with laminin in Fig. 6a and c.

Iron-responsive proteins in DRG and spinal roots of FRDA

Figure 8 illustrates the localization of ferritin in normal satellite cells (Fig. 8a–c) and a thicker rim of these cells in FRDA (Fig. 8d–f). The images in FRDA match the proliferation of satellite cells shown by routine cell stains (Fig. 1d) and S-100α immunocytochemistry (Fig. 1f). Mitochondrial ferritin could not be detected in any cell type of DRG, DR, or VR of FRDA patients.

Figure 9 illustrates the neuronal and non-neuronal localization of ferroportin in DRG, DR and VR. In normal DRG, the protein was detectable in the cytoplasm of

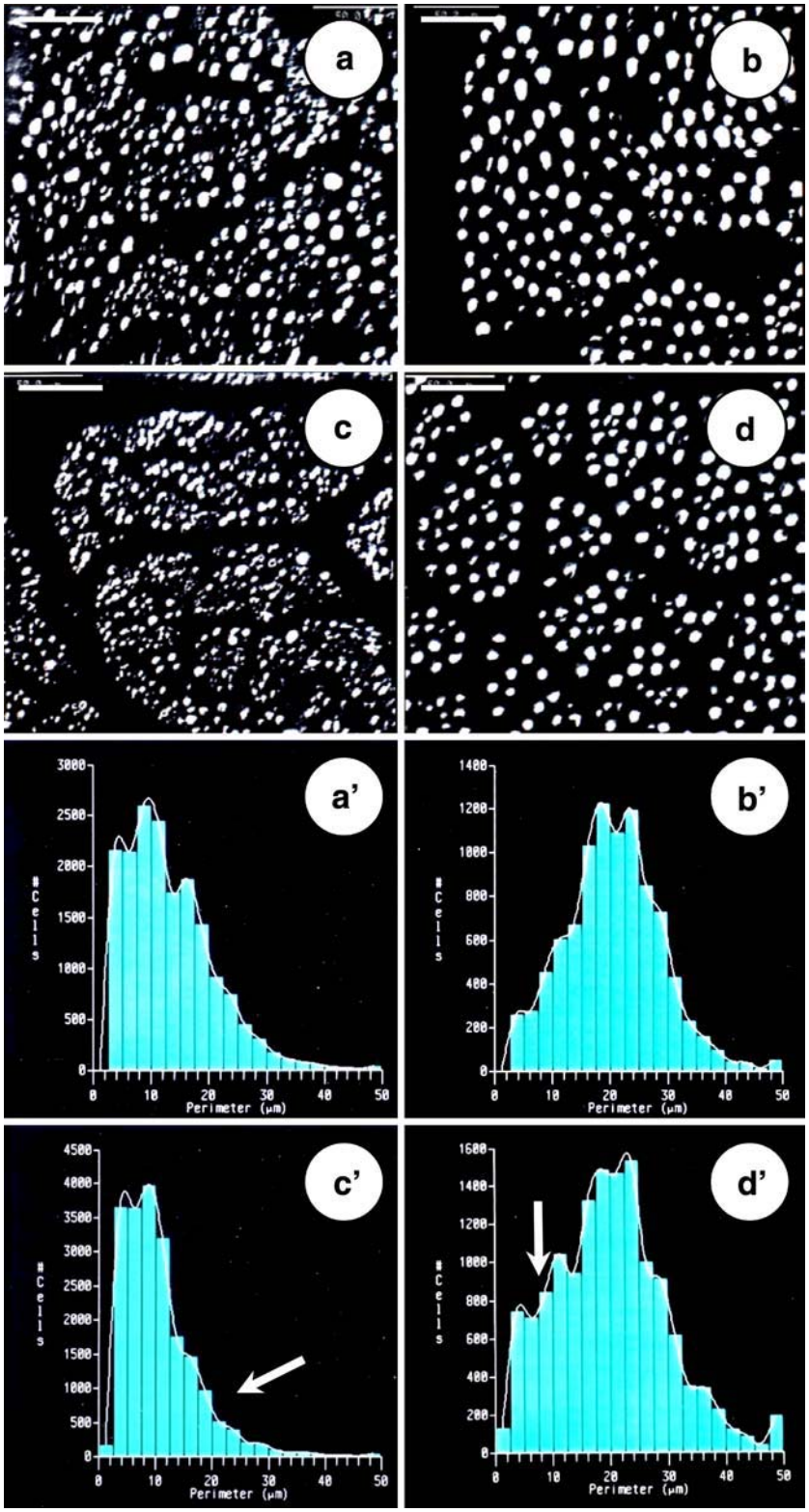

Fig. 3 Axons and pooled histograms of axonal perimeters in DR and VR of FRDA, and normal controls. **a**, **b** and **a′**, **b′** normal control, **c**, **d** and **c′**, **d′** FRDA. The *pooled histograms* in (**a′**), (**b′**), (**c′**), and (**d′**) correspond to the confocal images in (**a**), (**b**), (**c**), and (**d**). In the DR of FRDA, larger axons are infrequent while small-diameter axons remain (**c**). Fluorescence in VR shows no convincing differences between normal (**b**) and FRDA (**d**). The *pooled histograms* of 15 cases of FRDA and 11 normal controls confirm the loss of large axons in FRDA (*arrow* in **c′**). Surprisingly, FRDA also causes an increase in the number of small axons (*arrow* in **d′**). The ordinates (fibers counts) of the pooled histograms in (**a′**)–(**d′**) were adjusted to approximately equal peak height to aid visual comparison. Despite the obvious change in fiber perimeter, quantitative analysis reveals no significant numerical differences between FRDA and normal controls when expressed as a number of fibers/mm^2 area (see text). Laser confocal immunofluorescence with a monoclonal antibody to phosphorylated neurofilament protein (**a**–**d**). *Magnification bars* in (**a**)–(**d**), 50 μm

neurons and satellite cells (Fig. 9a, b), and the axoplasm of myelinated fibers of DR and VR (Fig. 9e, f). Antibodies to mouse [15] and human ferroportin peptides gave identical results. In FRDA, some neurons lost their ferroportin reaction product while they were still reactive for class-III-β-tubulin (Fig. 9c, d). Ferroportin immunoreactivity in satellite cells remained and persisted around nerve cells reaching complete atrophy (Fig. 9d). The loss of axonal

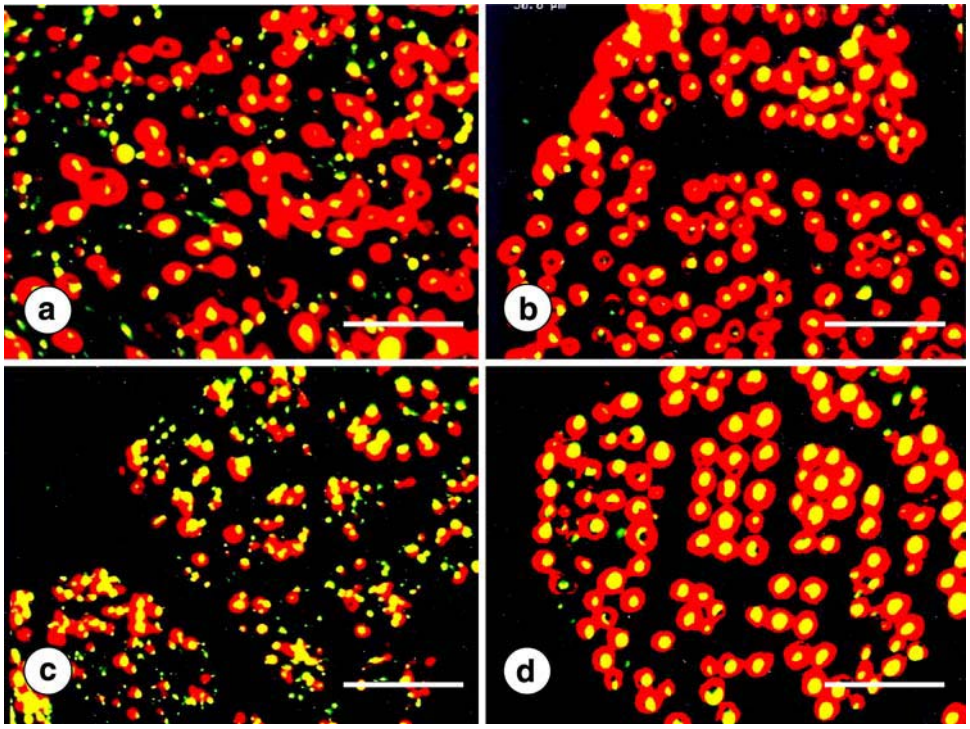

Fig. 4 Double-label immunofluorescence of PMP-22 and phosphorylated neurofilament protein in DR and VR of FRDA and a normal control. **a**, **b** Normal control, **c**, **d** FRDA, **a**, **d** DR, **b**, **d** VR, *green* and *yellow* (FITC), phosphorylated neurofilament protein; *red* (Qdot655), PMP-22. The DR of FRDA shows a great abundance of thinly myelinated nerve fibers (**c**) but lacks larger fibers when compared with a normal DR (**a**). VR in the normal control (**b**) and FRDA (**d**) are not distinctly different. Systematic quantitative analysis shows a significantly higher degree of myelination in the dorsal roots of FRDA ($p = 0.054$ at $\alpha = 0.05$). The degree of myelination in VR shows no statistical differences in myelination between normal controls and FRDA. *Magnification bars* 50 μm

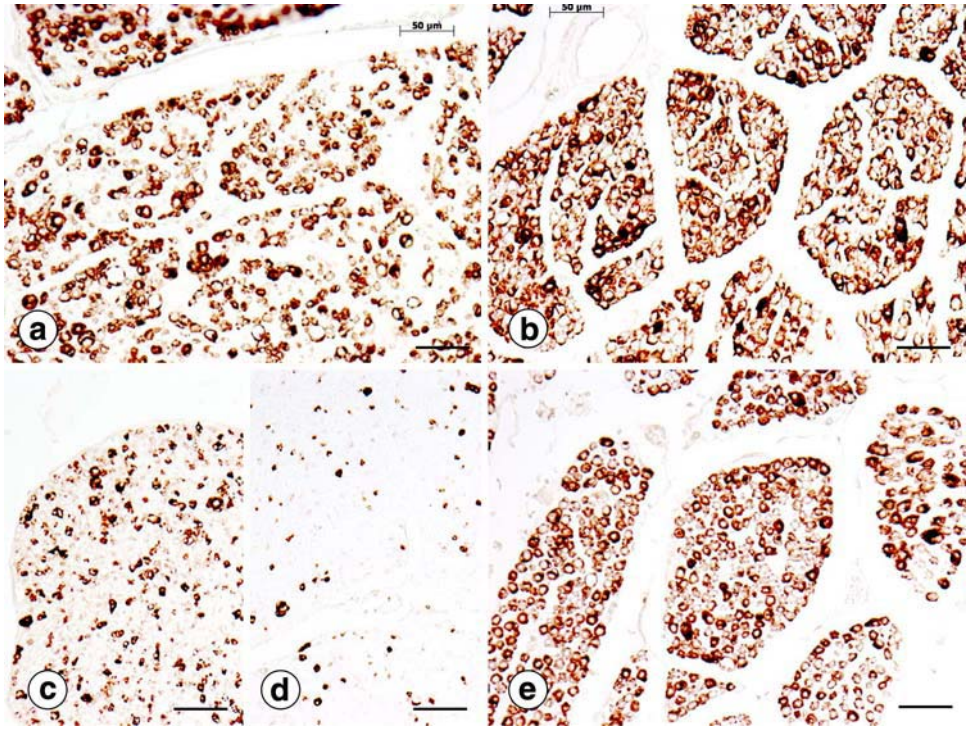

Fig. 5 S-100α-immunoreactivity in DR and VR of FRDA and a normal control. **a**, **b** Normal control, **c**–**e** FRDA, **a**, **c** and **d** DR, **b** and **e** VR. The DR of two patients with FRDA (**c**, **d**) show fewer reactive cells than normal and an overall reduction in cell size. The deficit is more severe in (**d**) than in (**c**), presumably due to longer survival of the patient (**d**). Ages of death and GAA trinucleotide repeats were as follows: **c** 10 years, 1,016/1,016; **d** 38 years, 934/249. Distribution and intensity of S-100α reaction product in VR of FRDA (**e**) do not differ from the normal control (**b**). *Magnification bars* 50 μm

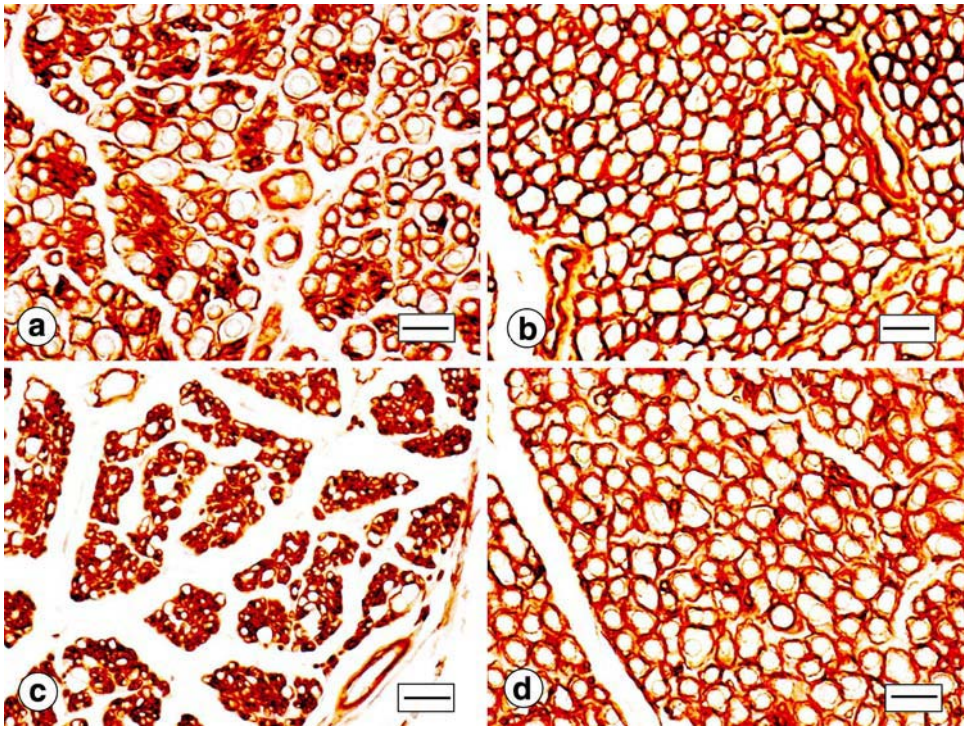

Fig. 6 Laminin immunoreactivity in DR and VR of FRDA. **a**, **b** Normal control, **c**, **d** FRDA, **a**, **c** DR, **b**, **d** VR. In the normal DR (**a**) rims of reaction product surround circular spaces that represent negative images of unstained myelinated axons. Interspersed, more compact regions of laminin reactivity correspond to clusters of normal thinner DR fibers. In the DR of FRDA (**c**), reaction product occurs almost exclusively in compact clusters that are crowded around numerous small circular voids. They probably represent thinly myelinated and unmyelinated axons. The VR of a normal control (**b**) and FRDA (**d**) do not differ in their appearance. Each *void* represents a myelinated fiber, and the arrangement is regular and honeycomb like. These microphotographs should be compared with the S-100α reaction products in DR and VR shown in Fig. 5. *Magnification bars* 20 μm

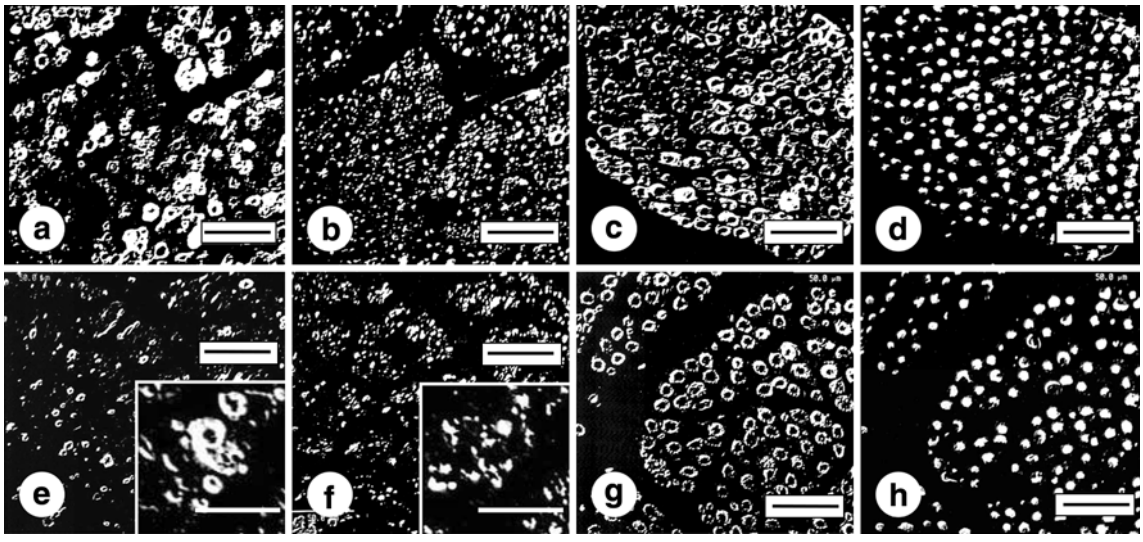

Fig. 7 Double-label immunofluorescence of DR and VR with antibodies to S-100α and neurofilament protein. **a**–**d** Normal control, **e**–**h** FRDA, **a**, **b**, **e**, and **f** DR, **c, d**, **g**, and **h** VR, **a**, **c**, **e**, and **g** S-100α (monoclonal antibody), **b**, **d**, **f**, and **h** neurofilament protein (polyclonal antibody). The matching images are **a** and **b**, **c** and **d**, **e** and **f**, and **g** and **h**. In FRDA, Schwann cells of DR are small and reduced in number (**e**) when compared with a normal dorsal root (**a**). The diffuse distribution of small and large axons in normal DR (**b**) is replaced by clusters of small axons around a few remaining larger axons (**f**). The matching images in the *insets* in (**e**) (S100α) and (**f**) (neurofilament protein) illustrate clusters of Schwann cell processes and axons, respectively. VR of a normal control (**c**, **d**) and FRDA (**g**, **h**) are not visibly different. Each axon appears surrounded by Schwann cell cytoplasm in a 1:1 relationship. *Magnification bars* 50 μm

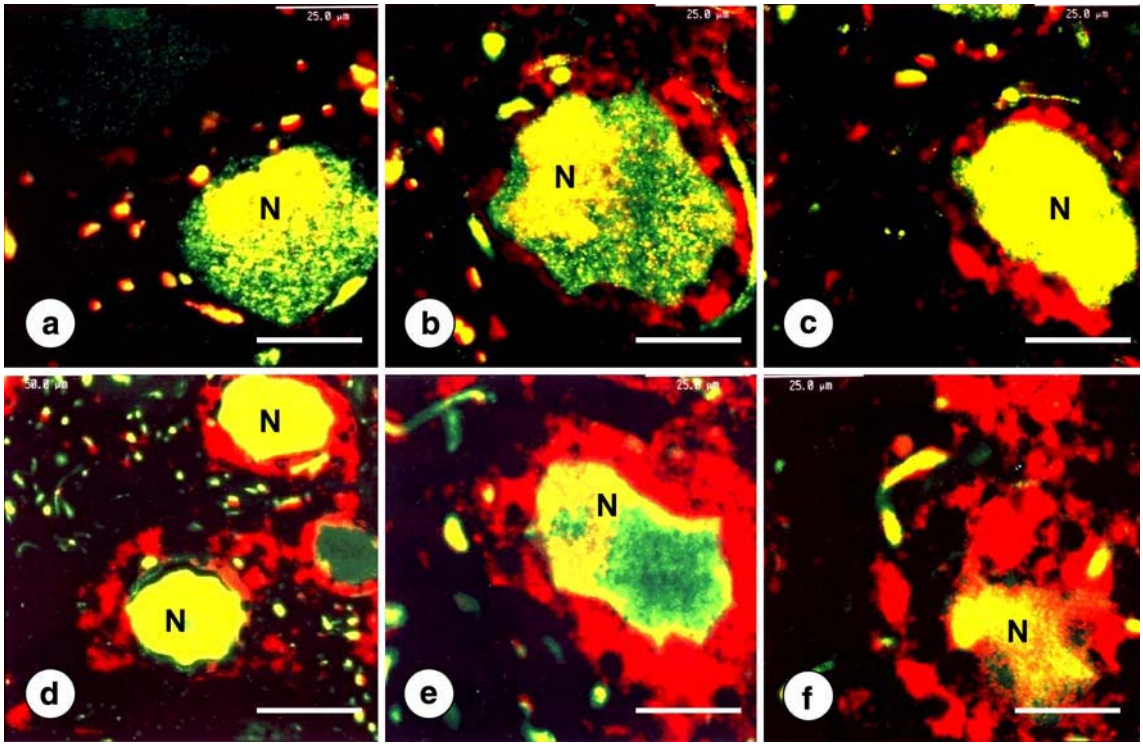

Fig. 8 Ferritin in DRG of FRDA and a normal control. **a–c** Normal control, **d–f** FRDA; double-label confocal immunofluorescence of class-III-β-tubulin (*yellow* FITC) and ferritin (*red* Qdot655). In the normal state, sparse ferritin reaction product occurs in satellite cells around many but not all neurons (*N* in **a–c**). In FRDA, the rim of ferritin-reactive satellite cells surrounding neurons is much thicker (*N* in **d–f**). A neuron (*N* in **f**) is approaching complete atrophy while surrounding satellite cells remain strongly ferritin reactive. *Magnification bars* 25 μm

ferroportin in DR of FRDA paralleled the disappearance of large myelinated fibers (Fig. 9g). Red reaction product between nerve fibers of DR in FRDA represents ferroportin in Schwann cells (Fig. 9g). Axonal ferroportin in VR remained unaffected (Fig. 9h).

High-definition X-ray fluorescence maps of iron in DRG and matching ferritin expression

Figure 10 displays HDXRF iron maps of two normal DRG and four DRG of patients with FRDA. Higher than normal iron signals occurred in a regional or diffuse manner. Copper and zinc signals were not elevated above controls. The iron map illustrated in Fig. 10c shows a subcapsular region of iron fluorescence that is 2–2.5 times higher than normal (Fig. 10a, b). In the maps of FRDA cases shown in Fig. 10e and f, increased iron fluorescence is present in very restricted areas. It is subcapsular in Fig. 10e and central in Fig. 10f.

Matching sections displaying ferritin immunoreactivity are shown below the iron maps. Two regions were selected from each DRG to show the extent of ferritin expression. In FRDA, the rectangles were placed to represent regions of high (continuous line) and low iron signal (interrupted line), respectively. The matching sections confirmed an overall reduction of neuronal size and crowding of ferritin-reactive satellite cells around smaller neurons in areas of higher than normal iron fluorescence (Fig. 10c–f).

Total iron in DRG

Total iron levels in DRG were 25.4 ± 10.3 μg/g wet weight (mean ± SD) in three patients with FRDA and 28 ± 13.4 (mean ± SD) in eight normal controls. The differences were not significant at $\alpha = 0.05$ ($p = 0.77$).

Discussion

The lesion of DRG in FRDA

Inoue et al. [13] made a systematic analysis of DRG in one patient with FRDA and reported that only one percent of neurons had a diameter over 54 μm. In a normal control, 17% of DRG neurons exceeded this measurement. It is widely accepted that large DRG neurons give rise to thick myelinated DR fibers, and a detailed anatomical analysis of posterior spinal rootlets of humans confirmed that these

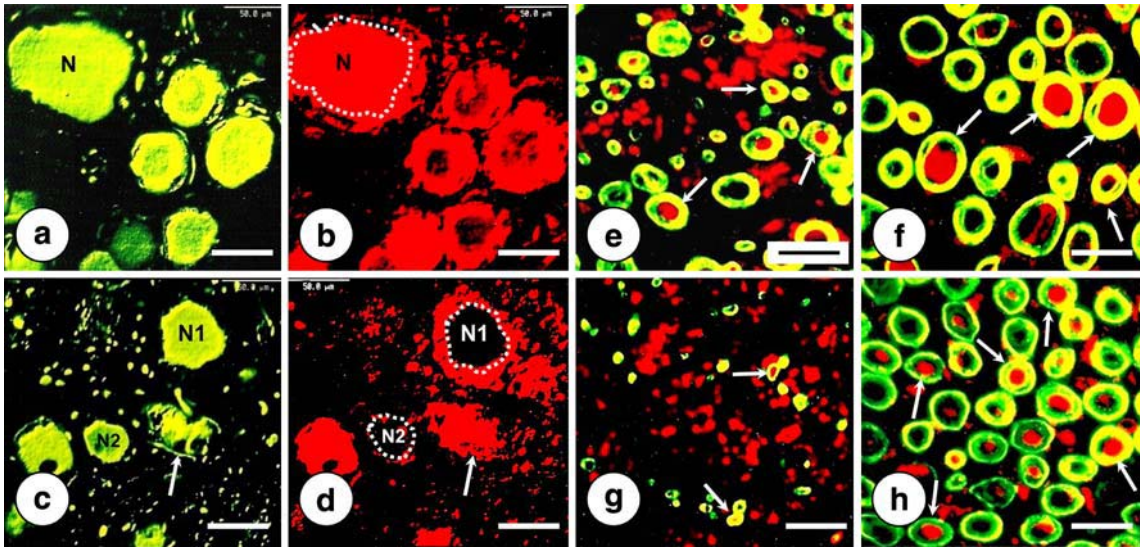

Fig. 9 Ferroportin in DRG, DR and VR of FRDA and a normal control. **a**, **b** Normal DRG, **c**, **d** DRG in FRDA, **e** normal DR, **f** normal VR, **g** DR in FRDA, and **h** VR in FRDA. **a**–**d** Double-label confocal immunofluorescence with anti-class-III-β-tubulin (*green* or *yellow* FITC) and ferroportin (*red* Qdot 655), **e**–**h** double-label confocal immunofluorescence of myelin basic protein (*green* or *yellow* FITC) and ferroportin (*red* Qdot 655). In normal DRG, ferroportin reaction product occurs in neuronal cytoplasm (*N* in **b**) and satellite cells. The interrupted line on neuron *N* in (**b**) outlines the limits of the class-III-β-tubulin-positive cytoplasm of the same neuron in (**a**). Reaction product outside this line in (**b**) may be attributed to satellite cells. In FRDA, the average size of nerve cells is smaller than in controls (**c**). Nerve cells shown as N1 and N2 in (**c**) and (**d**), respectively, have lost their cytoplasmic ferroportin. The atrophic neuron indicated by an *arrow* in (**c**) shows a thick layer of ferroportin, presumably due to the presence of several surrounding satellite cells (**d**). In normal DR (**e**), most large myelinated fibers (*arrows*) display axonal ferroportin reaction product. The *red* deposits between nerve fibers represent ferroportin-positive Schwann cell cytoplasm. Most VR axons are ferroportin-positive (*arrows* in **f**). In FRDA, only a few ferroportin-reactive DR axons remain visible (*arrows* in **g**). Red fluorescence outside axons in (**g**) may be attributed to Schwann cell cytoplasm. The VR of FRDA shown in (**h**) shows no difference in axonal ferroportin immunoreactivity (*arrows*) compared with a normal control (*arrows* in **f**). *Magnification bars* **a**–**d** 50 μm; **e**–**h** 25 μm

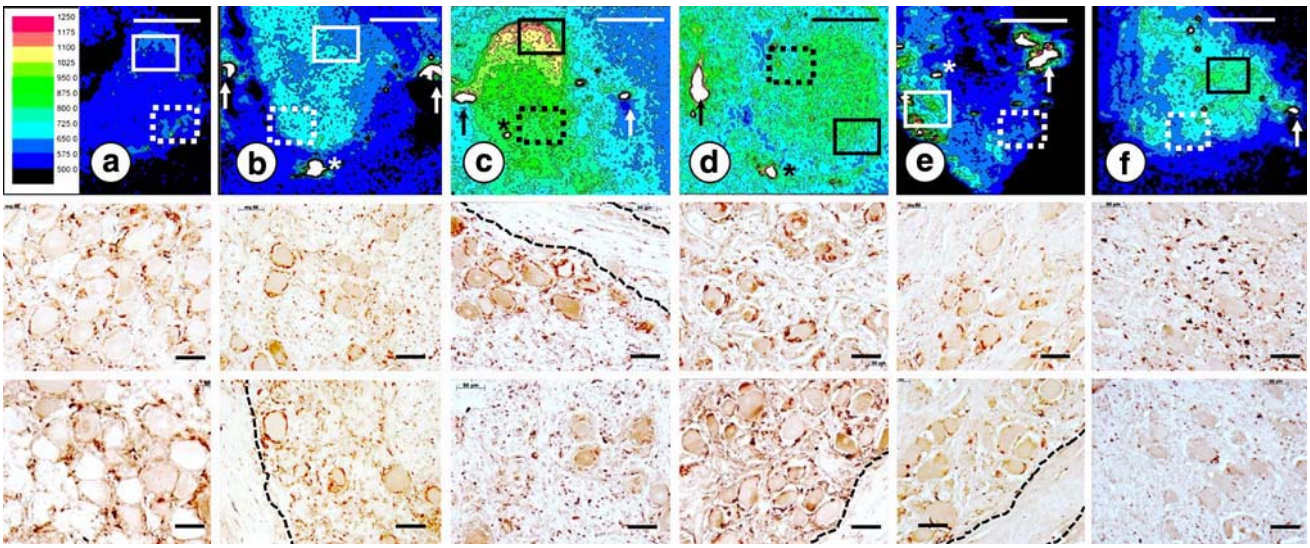

Fig. 10 HDXRF and iron maps of DRG and matching ferritin immunocytochemistry. **a**, **b** HDXRF of two normal DRG, **c**–**f** FRDA. Immunocytochemistry of ferritin is shown below the iron maps and the *upper row* corresponds to the *rectangles* with *solid borders* in the iron maps. The *lower row* of microphotographs corresponds to the *rectangles* with *interrupted lines*. The color scale in (**a**) represents iron levels measured as counts per 25 s. *Black* and *blue* indicate lower iron signals than *green*, *orange* or *red*. The *arrows* in (**b**), (**c**), (**d**), (**e**), and (**f**) show the placement of marker wires to guide the scanning mechanism of the instrument. *Asterisks* in (**b**), (**c**), (**d**), and (**e**) indicate instrument artifacts or contamination by iron-containing environmental particles. Elevated iron signals in HDXRF maps coincide with regions of small neurons that are surrounded by ferritin-reactive satellite cells. In some DRG, ferritin reaction product is most intense beneath capsules (*dotted lines*) (**c**, **d**). *Magnification bars* **a**–**f** 2 mm; all microphotographs, 50 μm

fibers are located dorsomedially just before entering the dorsal columns [32]. Static images of post mortem tissue after variable disease duration, however, do not allow the conclusion that the greater abundance of smaller neurons is the result of atrophy of larger ganglion cells, or that larger nerve cells are truly more vulnerable to the disease. The ganglion cells of normal DRG exhibit differential staining with antibodies to neuronal markers (Fig. 1b; ref. [21]) but large and small neurons alike appear to undergo destruction in FRDA (Fig. 1e). It may also not be justified to interpret the proliferation of satellite cells as a response to neuronal atrophy. It is equally possible that neuronal loss occurs due to a primary disease process in satellite cells. S-100α is a reliable marker for satellite and Schwann cells in vivo and in vitro (Figs. 1, 5; refs. [11, 25, 31, 34]) and can be used to track their differentiation from neural crest precursors [33]. In DRG of FRDA, the expression of this protein persists at the site of total neuronal collapse, and nodules of Nageotte remain strongly S-100α-reactive (Fig. 1f). This observation confirms that S-100α expression is independent of contact with neurons. Peculiarly, Schwann cells in DR lose much of their S-100α immunoreactivity pointing toward major differences between these cells and satellite cells in FRDA.

The lesions of spinal roots in FRDA

Loss of DRG neurons can be expected to cause a commensurate disappearance of their centrally projecting axons in DR, and this process accounts for the depletion of dorsal column fibers and afferent connections to the dorsal nuclei of Clarke and the gray matter of the dorsal horns. Loss of large myelinated fibers is clearly not the only change in DR of FRDA. The findings illustrated in Figs. 2, 3, 4, 5, 6, 7 point to a much more complex modification. Quantitative fiber counts must take into consideration that a major shift to smaller fibers has occurred and that axons have become more compact (Fig. 3c). The high resolving power of confocal double-label immunofluorescence microscopy of axonal and myelin proteins settles questions about the degree of myelination in DR of FRDA (Fig. 4c). The significantly higher ratio of myelinated to all stained axons in DR of FRDA is most likely due to remyelination of small regenerating axons. The loss of S-100α immunoreactivity in DR (Fig. 5c, d) cannot be explained by lack of contact with axons and must be reconciled with the retention of laminin (Fig. 6c). Despite its abundance, laminin distribution differs greatly from the normal state (Fig. 6c). A reasonable interpretation of the changes illustrated in Figs. 5c, d, 6c and 7e is as follows: The paucity S-100α reaction product represents a decrease of cytoplasm in the perikaryon of Schwann cells. In contrast, the number of processes with basal laminas remains unchanged or actually increases. The axon–Schwann cell ratio enlarges, and inappropriate myelination of newly formed, thin axons occurs (Fig. 7f). Hughes et al. [12] were at variance with Jitpimolmard et al. [14] and rejected axonal regeneration as an explanation for small-fiber abundance in DR. Hughes et al. [12] traced thin DR fibers in FRDA and found them to be continuous with intramedullary axons. Growth across the root entry zone seemed improbable. Thin axons ended in the dorsal horns of the spinal cord, and only a few entered the dorsal columns. In this study, transverse sectioning of the spinal cord and its attached roots precluded tracing of axons across the root entry zone.

Histograms of axonal perimeters suggest that VR are not entirely exempt from FRDA (Fig. 3d′).Two explanations are possible for this moderate abnormality. The excess of thin fibers (Fig. 3d′) may represent atrophy of efferent motor axons or the occurrence of afferent fibers in an atypical location (reviewed in ref. [22]). A few clusters of thin fibers also occur in VR of normal persons [22]. Their clinical significance is unknown. The observations on VR in FRDA may contribute to an improved clinicoanatomic correlation. Patients with FRDA often have moderately slow motor nerve conduction velocities, and some show fibrillations as an indication of muscle denervation [5]. Diffuse thinning of arms and legs is part of the clinical phenotype of FRDA, but is commonly attributed to severe general disability or "disuse". A more likely explanation is chronic denervation due to lesions of VR, a more distal motor neuropathy, or both. Interestingly, Mott [26] intended to illustrate an atrophic muscle spindle in FRDA in Fig. 1 of his 1907 paper, but the photomicrograph also shows a distinct group lesion of the adjacent muscle.

Evidence of iron dysmetabolism in DRG of patients with FRDA

Oxidative tissue damage in FRDA may be due to an excess of highly reactive, labile, or loosely bound iron, but it is unknown how frataxin deficiency would cause this increase. It is equally uncertain how lack of frataxin should lead to failure of well established iron homeostasis in humans. Post mortem changes probably preclude the direct determination of labile iron in DRG, but the effect of the reactive metal may be sought indirectly by examination of "downstream" effects, including iron histochemistry and immunocytochemistry of iron-responsive proteins. While iron stains were unrewarding, the combination of HDXRF signals and ferritin immunostaining allowed the conclusion that FRDA causes limited and regional increases of the metal in DRG and a biological response (Fig. 10).

The best known mechanism of tissue iron homeostasis is the coordinated biosynthesis of ferritin and transferrin

receptor 1 (TfR1). Iron excess strongly stimulates ferritin biosynthesis by releasing iron-regulatory proteins (IRP) from an iron-response element (IRE) in the 5′-untranslated region (5′-UTR) of ferritin messenger ribonucleic acid (mRNA). In contrast, TfR1 protein levels decline rapidly when iron rises and causes the dissociation of IRP from IRE in the 3′-UTR of TfR1 mRNA. Ferritin in this context is cytosolic, and its response in FRDA implies translational activation by iron in the cytoplasm of satellite cells. Frataxin deficiency, however, is primarily a problem of mitochondrial iron, and it is not surprising that mitochondrial ferritin has emerged as an important molecule in iron dysmetabolism of FRDA [3]. The protein is normally expressed only in testicular tissues, but Michael et al. [23] detected it in the hearts of patients with FRDA. It is unknown why FRDA does not cause the expression of mitochondrial ferritin in satellite cells or neurons of DRG.

Ferroportin is a relatively recent addition to the growing list of iron-handling proteins [1]. It shares an IRE in the 5′-UTR of its mRNA with ferritin, and translational stimulation by iron can be expected. In contrast to ferritin, however, ferroportin levels are also controlled by several other mechanisms that are unrelated to the interaction of iron and IRE. Michael et al. [23] and Koeppen et al. [17] reviewed the potential role(s) of this protein in myocardium [23] and dentate nucleus [17] of patients with FRDA. In extracerebral tissues, a circulating peptide, hepcidin, causes internalization and proteolysis of ferroportin but a similar control is unlikely for brain and spinal cord. In theory, circulating hepcidin may gain access to normal DRG and control the level of the protein in satellite cells. Ferroportin is a transmembrane protein that has been shown to export iron from a variety of cell types [29]. It is also expressed in the central nervous system [17, 24, 35], DRG, and spinal roots (Fig. 9), but a precise function in these tissues has not been established. In DRG, ferroportin is unique because of its dual localization in neurons and satellite cells. The co-localization of ferritin and ferroportin in satellite cells in FRDA suggests that these cells respond to cytoplasmic iron excess by coordinated biosynthesis. The putative result is protection against iron toxicity. Ferritin sequesters the metal, and ferroportin transfers it out of the cytoplasm. It may be suggested that this mechanism is not adequate in FRDA. Loss of ferroportin from some, but not all DRG neurons points to an additional problem with iron homeostasis that is unrelated to satellite cells (Fig. 9).

Ferritin and ferroportin immunoreactivity in satellite cells suggests that the control of tissue iron in DRG is the domain of satellite cells rather than cells of the monocyte/macrophage lineage. CD-68-reactive cells are present in normal DRG, but do not appear to participate in iron disposal in FRDA. This mechanism is consistent with the slow progression of the disease in DRG and the absence of inflammation. It differs from the cardiomyopathy of FRDA that commonly displays fiber necrosis and a reactive infiltration of the endomysium by CD68- and ferritin-reactive monocytes [23].

Many questions remain about iron in the pathogenesis of the lesions in DR and VR of FRDA. The intensity of immunocytochemical and immunofluorescent reaction products is only an approximate measure of ferritin and ferroportin expression. Loss of ferroportin-positive axons in DR (Fig. 9g) may be secondary to selective atrophy of DRG neurons (Fig. 9d) and not an indication of axonal iron dysmetabolism. In analogy, the persistence of ferroportin in axons of VR reflects the integrity of anterior horn cells (Fig. 9h). The effect of frataxin deficiency on iron-responsive proteins in DRG, DR, and VR will have to be studied by quantitative biochemical methods such as enzyme-linked immunosorbent assays and Western blotting [17, 23].

Schwann cells and satellite cells share an origin from the neural crest, but their expression of ferritin and ferroportin is not the same. Schwann cells do not show distinctly increased ferritin expression in DR of FRDA though they contain some ferroportin (Fig. 9g). The peculiar dissociation of S-100α and laminin expression in DR of FRDA requires further analysis. Peripheral neuropathy may change the laminin composition of Schwann cells that is normally a heterotrimer of α_2, β_1, and γ_1 subunits (reviewed in ref. [8]). The great modification of the axon–Schwann cell relationship in DR of FRDA may be analogous to the incorrect radial sorting in laminin-deficient animal models [8]. The observations presented here suggest that FRDA primarily affects satellite and Schwann cells and that loss of neurons and axons is a secondary event. The task remains to link the proposed vulnerability of two types of support cells to frataxin deficiency.

Acknowledgments The authors express their gratitude to the families of FRDA patients who agreed to donate tissues for research. Friedreich's Ataxia Research Alliance, National Ataxia Foundation, National Institutes of Health, and Neurochemical Research, Inc., have provided financial support. The work was completed in the laboratories of the Research Service, VA Medical Center, Albany, NY, USA. The authors thank the collaborating pathologists who performed extramural autopsies and harvested the samples for this investigation.

References

1. Abboud S, Haile DJ (2000) A novel mammalian iron-regulated protein involved in intracellular iron metabolism. J Biol Chem 275:19906–19912
2. Bielschowsky M (1934) Zur Kenntnis des Friedreich-Komplexes. Zeitschr ges Neurol Psychiat 150:373–404
3. Campanella A, Rovelli E, Santambrogio P, Cozzi A, Taroni F, Levi S (2009) Mitochondrial ferritin limits oxidative damage

regulating mitochondrial availability: hypothesis for a protective role in Friedreich ataxia. Hum Mol Genet 18:1–11
4. Campuzano V, Montermini L, Moltò MD et al (1996) Friedreich's ataxia: autosomal recessive disease caused by an intronic GAA triplet repeat expansion. Science 271:1423–1427
5. Caruso G, Santoro Perretti A et al (1983) Friedreich's ataxia: electrophysiological and histological findings. Acta Neurol Scand 67:26–40
6. Chen ZW, Gibson WM, Huang H (2008) High-definition X-ray fluorescence: principles and techniques. X-ray Optics Instrum:1–10. doi:10.1155/2008/318171
7. Davis MD, Kaufman S, Milstein S (1986) A modified ferrozine method for the measurement of enzyme-bound iron. J Biochem Biophys Methods 13:39–45
8. Feltri ML, Wrabetz L (2005) Laminins and their receptors in Schwann cells and hereditary neuropathies. J Peripher Nerv Syst 10:128–143
9. Friedreich N (1877) Ueber Ataxie mit besonderer Berücksichtigung der hereditären Formen. Nachtrag. Virchows Arch Pathol Anat Physiol Klin Med 70:140–152
10. Gibson WM, Chen ZW, Li D (2008) High definition X-ray fluorescence: applications. X-Ray Optics Instrum. doi:10.1155/2008/709692
11. Gonzalez-Martinez T, Perez-Piñera P, Díaz-Esnal B, Vega JA (2003) S-100 proteins in the human peripheral nervous system. Microsc Res Tech 60:633–638
12. Hughes JT, Brownell B, Hewer RL (1968) The peripheral sensory pathway in Friedreich's ataxia. Brain 91:803–818
13. Inoue K, Hirano A, Hasson J (1979) Friedreich's ataxia selectively involves the large neurons of the dorsal root ganglia. Trans Am Neurol Assoc 104:75–76
14. Jitpimolmard S, Small J, King RHM et al (1993) The sensory neuropathy of Friedreich's ataxia: an autopsy study of a case with prolonged survival. Acta Neuropathol 86:29–35
15. Knutson MD, Oukka M, Koss LM, Aydemir F, Wessling-Resnick M (2005) Iron release from macrophages after erythrophagocytosis is up-regulated by ferroportin 1 overexpression and down-regulated by hepcidin. Proc Natl Acad Sci USA 102:1324–1328
16. Koeppen AH (1998) The hereditary ataxias. J Neuropathol Exp Neurol 57:531–543
17. Koeppen AH, Michael SC, Knutson MD et al (2007) The dentate nucleus in Friedreich's ataxia: the role of iron-responsive proteins. Acta Neuropathol 114:163–173
18. Koeppen AH, Michael SC, Li D et al (2008) The pathology of superficial siderosis of the central nervous system. Acta Neuropathol 116:371–382
19. Lamarche JB, Côté M, Lemieux B (1980) The cardiomyopathy of Friedreich's ataxia: morphological observations in 3 cases. Can J Neurol Sci 7:389–396
20. Lambrior AA (1911) Un cas de maladie de Friedreich avec autopsie. Rev Neurol 21:525–540
21. Lawson SN (1992) Morphological and biochemical cell types of sensory neurons. In: Cott SA (ed) Sensory neurons: diversity, development, and plasticity. Oxford University Press, Oxford, pp 27–59
22. Lieberman AR (1976) Sensory ganglia. In: Landon DN (ed) The peripheral nerve. Chapman Hall, London, pp 188–278
23. Michael S, Petrocine SV, Qian J et al (2006) Iron and iron-responsive proteins in the cardiomyopathy of Friedreich's ataxia. Cerebellum 5:257–267
24. Moos T, Nielsen TR, Skjørringe T, Morgan EH (2007) Iron trafficking inside the brain. J Neurochem 103:1730–1740
25. Morrissey TK, Kleitman N, Bunge RP (1991) Isolation and functional characterization of Schwann cells derived from adult peripheral nerve. J Neurosci 11:2433–2442
26. Mott FW (1907) Case of Friedreich's disease, with autopsy and systematic microscopical examination of the nervous system. Arch Neurol Psychiatr 3:180–200
27. Nageotte J (1907) Recherches expérimentales sur la morphologie des cellules et des fibres des ganglions rachidiens. Rev Neurol 15:357–368
28. Pandolfo M (2008) Friedreich ataxia. Arch Neurol 65:1296–1303
29. Rice AE, Mendez MJ, Hokanson CA, Rees DC, Björkman PJ (2008) Investigation of the biophysical and cell biological properties of ferroportin, a multipass integral membrane protein iron exporter. J Mol Biol 386:717–732
30. Rouault TA, Tong WH (2008) Iron–sulfur cluster biogenesis and human disease. Trends Genet 24:398–407
31. Scarpini ES, Meola G, Baron P, Beretta S, Velicogna M, Scarlato G (1986) S-100 protein and laminin: Immunocytochemical markers for human Schwann cells in vitro. Exp Neurol 93:77–83
32. Sindou M, Quoex C, Baleydier C (1974) Fiber organization at the posterior spinal cord-rootlet junction in man. J Comp Neurol 153:15–26
33. Smith-Thomas LC, Fawcett JW (1989) Expression of Schwann cell markers by mammalian neural crest cells in vitro. Development 105:251–262
34. Stefansson K, Wollmann RL, Moore BW (1982) Distribution of S-100 protein outside the central nervous system. Brain Res 234:309–317
35. Wu LJ, Leenders AG, Cooperman S, Meyron-Holtz E, Smith S, Land W, Tsai RY, Berger UV, Sheng ZH, Rouault TA (2004) Expression of the iron transporter ferroportin in synaptic vesicles and the blood–brain barrier. Brain Res 1001:108–117